

2022-09

Energetics of tidally induced internal waves over isolated seamount

Stashchuk, Nataliya

<http://hdl.handle.net/10026.1/19918>

10.1016/j.wavemoti.2022.103014

Wave Motion

Elsevier

All content in PEARL is protected by copyright law. Author manuscripts are made available in accordance with publisher policies. Please cite only the published version using the details provided on the item record or document. In the absence of an open licence (e.g. Creative Commons), permissions for further reuse of content should be sought from the publisher or author.

Highlights

Energetics of tidally induced internal waves over isolated seamount

Nataliya Stashchuk and Vasiliy Vlasenko

- The study focuses on the tidal energy conversion to internal waves over an isolated seamount.
- Sensitivity runs were conducted in a wide range of the numerical grid resolution.
- The coarse grid models overestimate available potential energy converted to internal waves.

Energetics of tidally induced internal waves over isolated seamount

Nataliya Stashchuk and Vasiliy Vlasenko

The University of Plymouth, UK, Plymouth, Drake Circus, PL4 8AA

Abstract

Tidally generated internal waves over Rosemary Bank Seamount, North Atlantic, were investigated using the Massachusetts Institute of Technology general circulation model. The model results were validated against in-situ data collected during the 136th cruise of the RRS ‘James Cook’ in June 2016. The current study focuses on the sensitivity of the model output to the parameter settings. The estimates of the available potential energy integrated over the model domain were taken as a proxy for evaluating the sensitivity of the model results to the grid steps, horizontal and vertical viscosity, diffusivity, and mixing schemes. It was found that coarse grid models overestimate available potential energy converted to internal tides over seamounts. In fact, the energy conversion rate from barotropic to baroclinic tidal components is sensitive to the grid resolution. The reasons for this tendency are discussed in the paper.

Keywords:

Internal tide, Rosemary Bank Seamount, Numerical modelling

1. Introduction

2 The principal sources of the tidal energy conversion from barotropic to
3 baroclinic motions are located over oceanic ridges, continental slopes and
4 seamounts. These areas provide a basic income to the baroclinic wave en-
5 ergy, which ultimately converts into internal water mixing and provides the
6 conditions for setting the global oceanic circulation (Munk and Wunsch, 1998).

7 Analysis of the parameterization of internal wave effects for setting the
8 global oceanic stratification was recently estimated by MacKinnon et al.

(2017). The authors discussed tidally induced mixing over bottom obstacles and estimated how much tidal energy is radiated to the far-field with internal waves. The lee wave mechanism of internal wave generation was the focus of this study. This scenario takes place under supercritical tidal conditions when the tidal flow is strong enough to arrest the generated internal waves in the area of topographic features. The modelling results presented by MacKinnon et al. (2017) assume that further steps in the parameterization of water mixing are required for making the model predictions accurate. A very detailed analysis of the tidal energy conversion and contribution of higher baroclinic modes to the energy balance was conducted recently by Vic et al. (2019). Using a semi-analytical model, the authors found that higher baroclinic tidal modes can account for up to 27% of tidal energy conversion.

Note that coarse-grid ocean models cannot resolve internal lee waves and short-scale internal modes. As a consequence, these processes are missing in model energy estimates. However, the comparison of fine and coarse resolution model outputs can evaluate the effect of the sub-grid baroclinic process on the energy budget. The model settings can be the same except for the grid resolution in both cases. Such experiments help understand the role of small-scale processes in water mixing and energy budget.

The present paper focuses on Rosemary Bank Seamount (RBS) located in the North Atlantic, Figure 1. This case study aims to understand the sensitivity of model predictions to the model settings. 136th cruise of the RV "James Cook" was conducted in the RBS area in May-June 2016 (hereafter JC136). The data collected during this cruise are considered in the present paper. Specifically, we refer to the temperature, salinity, temperature and velocity profiles recorded at three CTD-LADCP stations (Connectivity-Temperature-Depth, Lowered-Acoustic-Doppler-Current-Profiler). The positions of oceanographic stations are shown in Figure 1 a.

Theoretical analysis of the tidally induced internal waves around RBS was reported in (Stashchuk and Vlasenko, 2021). It was found there that internal wave dynamics, specifically, the wave generation and their propagation over RBS, can be treated in terms of two waveguides located in the seasonal and main pycnoclines, Figure 1 a. Specifically, the tidal flow interacting with a cluster of volcanic origin tall bottom cones located at the RBS summit (see Figure 1 a) generates short-scale internal waves in subsurface 100m thick seasonal pycnocline layer. Below 800m depth, i.e. in the main pycnocline, Figure 1 b, oscillating tidal flow generates bottom trapped sub-inertial internal waves propagated counterclockwise around RBS.

The numerical experiments reported in (Stashchuk and Vlasenko, 2021) revealed a good agreement between the model and observational data. The present study is based on the concept of two waveguides reported in the paper mentioned above. The intensification of the baroclinic tidal signal in the surface and bottom layers is evident both in observations (Figure 2 a,b) and the model outputs (Figure 2 c,d).

The present study focuses on the requirements that should be applied to large-scale modelling. In many global ocean models, the horizontal grid resolution is relatively coarse, several kilometres in the best-case scenario. The model requirements for simulations of tidally induced baroclinic motions are more demanding. In many cases, the horizontal grid resolution should be 100 m or less for accurate replication of generated internal waves. The global oceanic models are incapable of simulating internal tides with such grids on global and regional scales (Robertson, 2006). We consider the RBS area as a case study in the context of broader applications of the modelling efforts.

Structure wise, the paper is arranged as follows. It starts with the model description. This section is followed by a discussion of the baroclinic tidal energy estimation method. The grid resolution and the turbulent mixing parameterizations are discussed in the section "Model results". Finally, the principal outcomes of the study are formulated in the concluding section.

2. The model

The modelling experiments were conducted using the fully non-linear non-hydrostatic Massachusetts Institute of Technology general circulation model (MITgcm) (Marshall et al., 1997). The model domain, Figure 1 a, included a 815×698 numerical grid with horizontal resolution 115 m in its central part. A telescopic increase of the spatial resolution was arranged by adding extra 128 grid points to the lateral boundaries of the calculation area. In doing so, a smooth increase of the horizontal resolution from 115 m in the central part to $2 \cdot 10^8$ m at the periphery allowed to avoid the wave reflection from the model boundaries. The water depth was restricted by 2000 m isobath in the vertical direction. The vertical grid step was ten metres in all numerical experiments.

The shaved cell method for the topography interpolation was used in the present study. Its advantage, compared to the traditional full step representation, is in the reduction of numerical errors induced by the incorrect bathymetry interpolation. This problem was discussed by Adcroft et al.

83 (1997). It was demonstrated there that the shaved cell method for the to-
 84 pography interpolation shows a substantial improvement in the consistency
 85 of the model results with the observational data compared with the tradi-
 86 tional full step topography representation. The partial cell capability can be
 87 used with the variable parameter called in the MITgcm as *hFacMin* (value
 88 between 0 and 1). It corresponds to the minimum fractional size of the cell.
 89 In the present calculation, we have been using *hFacMin*=0.2.

90 The tide forcing was activated in the model by a tidal potential added
 91 to the right-hand side of the momentum balance equations. The details of
 92 the method are described in (Vlasenko and Stashchuk, 2021). Considering
 93 that M₂ tidal signal predominates in the RBS area, we restricted our analysis
 94 using only principal semidiurnal tidal forcing. The tidal input parameters
 95 were set using the data taken from the inverse tidal model TPXO 8.0 (Egbert
 96 and Erofeeva, 2002). The model was run with a steady, uniform horizontal
 97 stratification assuming no initial horizontal pressure gradients.

98 The Richardson number dependent parametrization, PP81, was used for
 99 the coefficients of vertical viscosity A^h and diffusivity K^h (Pacanowski and
 100 Philander, 1981). The details are as follows:

$$\begin{aligned}
 A^v &= \frac{A_0^v}{(1+a\text{Ri})^n} + A_b^v, \\
 K^v &= \frac{A^v}{(1+a\text{Ri})} + K_b^v.
 \end{aligned} \tag{1}$$

101 Here *Ri* is the Richardson number, $\text{Ri} = N^2(z)/(u_z^2 + v_z^2)$, and u and v are
 102 the components of zonal and meridional horizontal velocities, respectively.
 103 The background mixing/viscosity model parameters A_b and K_b were set at
 104 the minimum level to provide the conditions for internal waves generation
 105 and propagation: $A_b^v = 10^{-5} \text{ m}^2 \text{ s}^{-1}$ and $K_b^v = 10^{-5} \text{ m}^2 \text{ s}^{-1}$. The adjustable
 106 parameters were: $A_0^v = 1.5 \cdot 10^{-2} \text{ m}^2 \text{ s}^{-1}$, $a=5$ and $n=1$. This set of model
 107 parameters revealed the excellent performance of the MITgcm in replication
 108 of tidally generated internal waves (Stashchuk et al., 2014; Stashchuk and
 109 Vlasenko, 2017; Vlasenko et al., 2014, 2018).

110 The PP81 parameterization increases the coefficients A^v and K^v in the
 111 areas with small Richardson numbers, which dumps shear instabilities and
 112 smooths inverse water stratification produced by breaking internal waves. It
 113 also allows setting the upper limit of the vertical viscosity coefficient A_{max}^v .
 114 In this study A_{max}^v was taken at the level of $0.1 \text{ m}^2 \text{ s}^{-1}$.

115 The vast majority of the model runs in this study were conducted for the
 116 time interval of six days (144 hours) with the constant horizontal viscosity

117 A^h and diffusivity K^h coefficients equals $0.5 \text{ m}^2 \text{ s}^{-1}$. Additional sensitivity
118 runs were done in a wide range of diffusivity/viscosity parameters. They are
119 discussed below.

120 Computing wise, one-hour outputs were arranged for all three-dimensional
121 fields. In addition, vertical profiles of temperature and horizontal velocities
122 were recorded with one-minute sampling at some selected points. Their po-
123 sitions coincide with the CTD-LADCP stations.

124 3. Tidal energy estimation method

125 The tidal energy conversion rate from barotropic to baroclinic component
126 depends on many factors. They are the intensity of the tidal flow, water
127 stratification, the shape of bottom topography, background mixing processes,
128 etc. The sink of tidal energy to internal waves and ultimately to water mixing
129 can be quantified in terms of internal tidal energy generated over the bottom
130 topography.

131 In many cases, it is not easy to separate the barotropic tidal signal from
132 the baroclinic one. Specifically, this is true when velocities are recorded
133 over an inclined three-dimensional bottom topography. In this case, the
134 separation procedure can introduce a significant error.

135 The residual currents generated by tides can lead to extra uncertainty in
136 the calculations of a vertical mean tidal velocity. Specifically, this concerns
137 the case of bottom trapped waves. Such a case was reported by Lerczak et
138 al. (2003) who studied internal wave dynamics at the Mission Beach (USA).
139 Analysing the ADCP data, they found differences in the structure of along-
140 shore and cross-shore tidal currents. The authors pointed out that separating
141 the barotropic tidal signal from the baroclinic one should be used with cau-
142 tion, particularly in regions with significant topographic variations. Note
143 that the estimates of available potential energy produced by tides are less
144 sensitive to the barotropic component. The analysis presented below is based
145 on the estimation of the APE.

146 Several methods are used for the APE calculations. A comprehensive
147 analysis of the procedures applied to internal wave fields was presented by
148 Kang and Fringer (2010). Three commonly used methods for the APE esti-
149 mates suggested by Lorenz (1955), Gill (1982), and Holliday and McIntyre
150 (1981) are considered in this paper. It was found that the method reported
151 by Holliday and McIntyre (1981) is the most accurate in the calculation of
152 the APE for internal waves. Their technique is based on the Taylor series

analysis. The recommended formula for the APE estimates is as follows:

$$\text{APE} = \frac{g^2 \rho'^2}{2\rho_0 N^2} + \frac{g^3 (N^2)_z \rho'^3}{6\rho_0^2 N^6} + O(\rho'^4). \quad (2)$$

Here ρ' is the perturbation of density to its equilibrium state.

Algorithm (2) was used in this paper. The APE calculations were conducted every one hour using the model outputs. The graphs are presented below in the following sections. Technically, the APE was calculated by vertical and horizontal integration over the whole model domain. The quadratic polynomial fit that includes the three nearest grid points best fits for the volume integrated APE and presents the long-term trend

4. Model results

The sensitivity of the model output to the horizontal and vertical grid resolution is reported in this section. The principal point of this study is: what the horizontal and vertical grid steps Δx and Δz should be taken to resolve the baroclinic tidal processes correctly? Vitousek and Fringer (2011) have shown that the ability of the model to reproduce small-scale nonhydrostatic physical processes depends on the leptic ratio coefficient, $\lambda \equiv \Delta x/h_1$. Here h_1 is the depth of the interface/pycnocline. For an accurate replication of the internal wave dynamics produced by non-hydrostatic models, the value of the leptic ratio λ should be at the level of $O(1)$ (Vitousek and Fringer, 2011).

Considering these requirements, one should mention that the water stratification in the RBS area has two principal elements shown in Figure 1 b: a shallow 100-metre depth seasonal pycnocline and the main pycnocline located below 1000 m depth. The latter is weaker but occupies a much larger part of the water column.

Numerically wise, both values of h_1 for seasonal and main pycnoclines can be taken to estimate the leptic ratio. These estimates can help in the choice of the model resolution. The principal question is: what processes should be replicated by the model? The fine resolution modelling allows considering a wide variety of small-scale dynamics, both short-scale internal waves developed in seasonal pycnocline and bottom trapped internal tidal waves. These requirements are not always possible for global-scale models. We consider a range of grid settings to illustrate models' abilities to replicate the wide-scale baroclinic tidal motions. The study discusses fine-scale resolution

186 model experiments and analyses the coarser grid runs used in global ocean
187 models.

188 4.1. Sensitivity to the grid resolution

189 An example of the model sensitivity to the grid resolution is shown in
190 Figure 3. The model temperature time-series at station 32 (Figure 1 a) was
191 calculated with different horizontal grid steps, 111.75 m, 463 m, and 926 m.
192 They are presented in panels a, b, and c of Figure 3, respectively. This figure
193 reveals that the ability of the model to capture short internal waves in the
194 upper seasonal pycnocline layer decreases with the increase of horizontal grid
195 steps. However, the numerical scheme still works well with coarser resolution
196 and reproduces long wave oscillations. Note that long-term wave amplitudes
197 increase with the increase of the horizontal grid steps.

198 How sensitive are the tidally induced baroclinic motions and water mixing
199 to the model resolution? The coarser grid model predictions of internal tidal
200 energy could differ from that estimated in the fine-resolution experiments.
201 The influence of the horizontal step on the value of APE is illustrated in
202 Figure 4 a. Here a six-day time series of the depth-integrated model domain
203 APE calculated for the horizontal resolution $\Delta x = \Delta y = 111.75$ m, 463 m, and
204 926 m are presented. The parameters $A^h = K^h$ in these experiments were
205 $0.5 \text{ m}^2 \text{ s}^{-1}$, and the vertical resolution Δz was equal to 10 m.

206 The common feature of all three graphs is the evidence of tidal periodicity.
207 The fit curves to these periodical oscillations show the steady growth of the
208 APE. However, after six days of tidal motion, the system ultimately arrives
209 at a stationary state.

210 The coarser grids usually dump short internal waves, which reduces the
211 APE in the numerical predictions. At the same time, coarser grids do not
212 affect the generation of long internal waves, which are more energetic than
213 short-scale waves. To have some quantitative estimates, a series of numeri-
214 cal experiments with different grid resolutions, horizontal and vertical, was
215 conducted to study the sensitivity of the model outputs to the model grid
216 parameters.

217 The APE time series for a wide range of model resolution with horizontal
218 grid steps from 115 m to 926 m, and vertical grid steps from 5 m to 20 m are
219 presented in Figures 4 a and 4 b. These figures show the spin-up of the model
220 over about 150 hours. The model comes to a stationary regime at the end
221 of this time interval, although the domain integrated APE is sensitive to the
222 model resolution. It is generally higher at coarser grids.

223 There are several explanations for this result. The first one can be found
 224 considering the domain volume. The latter is sensitive to the grid resolution.
 225 It varies with changing vertical and horizontal model grid steps, Figure 4 c
 226 and 4 d. The MITgcm is a Z -coordinate model which approximates the
 227 bottom as a step-wise function. The bottom topography in Z -coordinate
 228 models and the total water volume varies depending on the grid resolution.
 229 For instance, the total volume of water in the model domain for the coarser
 230 experiment shown in Figure 4 exceeds the fine-resolution volume for more
 231 than 2%. In addition, the topography in the coarser grid is steeper. The
 232 increase of the bottom steepness results in the generation of more energetic
 233 bottom-trapped internal waves, Figure 3.

234 The confirmation of the APE growth due to roughening of topography is
 235 seen in Figure 4 b. It shows the domain-integrated APE time series for three
 236 different vertical grid steps, 5 m, 10 m, and 20 m. Quantitatively, decreasing
 237 the vertical resolution in Z -coordinate models increases the water volume in
 238 the regions of sloping topography. As a result, the total APE calculated at
 239 coarser grids is higher, Figure 4 d. Making the vertical resolution thinner
 240 leads to improvements in the replication of the bottom flow dynamics.

241 Considering some local characteristics (not the domain integrated), the
 242 sensitivity of the model output to the grid resolution can be more detailed.
 243 Two examples of this sensitivity are shown in Figure 5. The model predicted
 244 temperature calculated at the positions of CTD stations 31 and 33 shows the
 245 consistency of all time-series considered with different horizontal and verti-
 246 cal grid resolutions. The tidal nature of vertical oscillations is clearly seen in
 247 these records. All curves reveal in-phase tidal periodicity. The amplitudes of
 248 vertical oscillations for all model outputs are also comparable. That could
 249 be evidence that coarse grid models can capture the main energy contributor
 250 with acceptable accuracy. At the same time, decreasing horizontal and verti-
 251 cal model resolution introduces some more details that can be very important
 252 for predicting local marine environment parameters.

253 4.2. *Sensitivity to horizontal mixing parameterization*

254 The time series of the model predicted APE calculated for different model
 255 settings, e.g. diffusivity, viscosity and grid resolution, are compared in this
 256 section. By making the grid finer, at some stage the model output starts to
 257 be insensitive to further reduction of the grid step.

258 Figures 6 shows the domain integrated APE and its best fit for different
 259 values of the viscosity coefficients: 0, 0.01, 0.5, $50 \text{ m}^2 \text{ s}^{-1}$. All curves presented

here show that the tidal energy increases gradually after the model starts. The spin-up period, 150 hours, is shown in Figure 6. The system becomes stationary when the pumping tidal energy is balanced by dissipation. As we found, the model predicted volume integrated APE capacity in the area does depend on the horizontal mixing parameterization. For the horizontal mixing/viscosity coefficients between $0.01 \text{ m}^2 \text{ s}^{-1}$ and $50 \text{ m}^2 \text{ s}^{-1}$ the APE level varies in the range of 100 %, Figure 6. This fact should be taken into account in the interpretation of large-scale circulation modelling results.

4.3. Experiments with vertical mixing schemes

In large-scale models, the energy cascading along the spectrum is generally provided, introducing parameterization schemes for vertical viscosity and diffusivity. One of them is the Richardson number based parameterization (1) included in the MITgcm package as a standard option. It shows a good performance for internal tide modelling in many studies, e.g. Vlasenko et al. (2014, 2016, 2018); Vlasenko and Stashchuk (2018).

Field measurements (Polzin et al., 1997) have revealed that vertical mixing does not occur uniformly over the oceans. It is normally enhanced near rough topographies due to the generation of internal waves that convert to turbulence. The lower level background mixing develops at the level of $\sim 10^{-5} \text{ m}^2 \text{ s}^{-1}$ over the whole ocean interior (Ledwell et al., 1998; Gregg, 1989). This value can be three orders of magnitude larger **over rough topography features**, (Polzin et al., 1997). To have a comparison, the results presented below show the model outputs calculated for two MITgcm build-in vertical mixing schemes. In all experiments, the horizontal grid resolution was 463 m.

4.3.1. Richardson number dependent scheme PP81

The Richardson number dependent parameterization for vertical mixing (1) was used in this study. The value $0.1 \text{ m}^2 \text{ s}^{-1}$ of the maximum permissible viscosity coefficient A_{max}^v was taken in this study. This requirement is applied in the MITgcm setting for the areas with strong vertical mixing, assuming possible density inversions. Note that the background turbulent mixing was set at the level of $A_b^v = 10^{-5} \text{ m}^2 \text{ s}^{-1}$ and $K_b^v = 10^{-5} \text{ m}^2 \text{ s}^{-1}$ in the whole area.

The sensitivity of the model outputs to the viscosity coefficient A_{max}^v was checked by changing this parameter within a two-order range. The result is shown in Figure 7. It illustrates that the increase of A_{max}^v from 0.001 to $0.1 \text{ m}^2 \text{ s}^{-1}$ leads to stabilizing of the model output. Comparing the time

series of temperature records calculated for Station 32 with different A_{\max}^v coefficients, Figures 7 a and 7 b, indicates that the choice $A_{\max}^v=0.1 \text{ m}^2 \text{ s}^{-1}$ shows a more stable model output.

4.3.2. KL10 mixing scheme

Klymak and Legg (2010) developed an original mixing scheme that is focused on the effect of breaking internal waves and does not include the Richardson-number criterion. This scheme assumes that energy dissipation is governed by the equivalence of the density overturning scales to the Ozmidov scale. Eddy diffusivity and viscosity are estimated using the Osborn relation (Osborn, 1980). This method yields a simple parameterization $Kz = 0.2L_T^2N$, where L_T is the size of vertical density overturns. This method is included in the MITgcm as the KL10 package. It was scrutinized by Klymak et al. (2013) that this parameterization does not account for shear-driving mixing.

A series of experiments were conducted in the present study with KL10 mixing scheme. An example of typical time series of the APE calculated for station 32 is shown in Figure 7 c. For the comparison, panels a and b show similar time series calculated using the PP81 scheme with different maximum permissible viscosity coefficients A^v . All other model parameters were the same in these experiments.

Note that at a local scale, a two-order decrease of the maximum vertical viscosity coefficient results in the appearance of instabilities that are visible in the time series, Figure 7 b. Comparison of Figures 7 a and 7 b indicates that the choice $A_{\max}^v=0.1 \text{ m}^2 \text{ s}^{-1}$ is the more realistic one producing a more stable vertical structure (without inversions) usually observed in the ocean. The KL10 parameterization reproduces both long-period internal waves in the bottom layer and short-period waves in the surface layer quite successfully, Figure 7 b, although the signal looks less regular than that produced by the PP81 scheme, Figure 7 a.

Figure 8 b shows the APE time series obtained with the PP81 and KL10 schemes. Both APE curves are close to each other over 93 hours of the model run. However, after eight tidal cycles, the APE calculated using the KL10 scheme continues to grow above the already saturated APE level achieved by the PP81-scheme.

330 5. Discussion and conclusions

331 Tidal energy conversion from barotropic to baroclinic components is one
 332 of the principal driving forces of the global ocean mixing and meridional
 333 overturning circulation (Munk and Wunsch, 1998). This process is still not
 334 well resolved in global ocean models. Specifically, the question is to what
 335 extent the tidal energy conversion is sensitive to the models' settings. Grid
 336 resolution, vertical turbulent mixing parameterization, and horizontal viscos-
 337 ity/diffusion settings are critical for a robust model prediction.

338 In previous studies, the authors achieved a good agreement between the
 339 model outputs and field observations (Stashchuk et al., 2014; Stashchuk and
 340 Vlasenko, 2017; Vlasenko et al., 2014, 2018). In this paper, a similar range of
 341 input model parameters is used. In the RBS area, the comparative analysis
 342 of model results and in situ data collected during JC136 cruise was reported
 343 in (Stashchuk and Vlasenko, 2021). The consistency of the model outputs
 344 with the in-situ collected data was demonstrated. The present paper con-
 345 sideres the problem in a broader context, assuming that large-scale numerical
 346 models usually use coarse numerical grids and can not include fine-scale baro-
 347 clinic processes. The present paper estimates the possible effect of numerical
 348 grid resolution and turbulent mixing parameterization schemes on the model
 349 output. The principal aim was to find the range of the model applicability
 350 and its sensitivity to the input parameter settings.

351 It was found that the increase of the grid step leads to a damping of
 352 the generation of short internal waves. This result was entirely expected,
 353 assuming higher numerical viscosity at coarser grids. A surprising outcome
 354 was the increase of the domain integrated APE at coarser numerical grids.
 355 The answer was found in terms of the model topography variations presented
 356 at different grid resolutions. Z -coordinate numerical models reproduce the
 357 bottom topography steeper at coarser grids, affecting the model performance
 358 and intensifying the generated waves.

359 The estimates of the tidally induced kinetic energy (K) accumulated in
 360 the area over one tidal cycle has shown the following results: $K = 3.814 \cdot 10^{13}$ J
 361 for the grid $\Delta x = \Delta y = 115.75$ m, $K = 3.8337 \cdot 10^{13}$ J for the grid $\Delta x =$
 362 $\Delta y = 463$ m, and $K = 4.0357 \cdot 10^{13}$ J for the grid $\Delta x = \Delta y = 926$ m. The
 363 vertical resolution dz and the background horizontal viscosity A_b^v were the
 364 same in all these experiments, i.e. $dz = 10$ m and $A_b^v = 0.5 m^2 s^{-1}$, respec-
 365 tively. Thus, it was found that both available potential energy and the kinetic
 366 energy increase in the model outputs on coarser grids.

367 The energy conversion rate from barotropic tidal component to internal
 368 waves in the RBS area was estimated. The calculations were conducted using
 369 the methodology suggested by Kelly et al. (2010); Zhang et al. (2017). The
 370 energy conversion EC for the domain $L_x \times L_y$ was calculated as:

$$EC = \int_0^{L_x} \int_0^{L_y} \langle p' \vec{U} \nabla H \rangle dx dy. \quad (3)$$

371 Here $\langle . \rangle$ means the time-averaging over one tidal cycle, \vec{U} is the depth-
 372 averaged horizontal velocity, and p' is the wave-induced pressure perturba-
 373 tion. It was found that $EC = 3.35 \cdot 10^8$ W for a grid $\Delta x = \Delta y = 115.75$ m,
 374 $EC = 3.32 \cdot 10^8$ W for the grid resolution $\Delta x = \Delta y = 463$ m, and $EC = 2.97 \cdot 10^8$ W
 375 for the grid $\Delta x = \Delta y = 926$ m. The vertical step for all considered experi-
 376 ments was the same, equals $\Delta z = 10$ m. Our experiments clearly show that
 377 the energy conversion rate from surface tides to baroclinic motions is under-
 378 estimated in coarser grid experiments.

379 A similar analysis of the sensitivity of the energy conversion rate to the
 380 horizontal grid spacing was conducted by Niwa and Hibiya (2011) (for Global
 381 Ocean) and Zilberman et al. (2009) (for the Mid-Atlantic Ridge). These au-
 382 thors used quite a different numerical approach than applied in the present
 383 paper. Specifically, the terrain-following sigma-coordinate hydrostatic mod-
 384 els were applied to these calculations. It was found there that the tidal energy
 385 conversion rate integrated over the global ocean (Niwa and Hibiya, 2011) and
 386 local area in the Brazil Basin (Zilberman et al., 2009) increases with the re-
 387 duction of the model grid spacing. This conclusion is in line with the results
 388 reported here obtained by using the z -coordinate MITgcm model.

389 A methodological outcome from this study is that simple estimations of
 390 the available potential energy and the total kinetic energy generated by the
 391 tides over RBS show the increase of these values on coarser model grids,
 392 Figure 6 a and b. At the same time, the estimates of the energy conversion
 393 rate from barotropic to internal tide reveal that the coarser grids reduce the
 394 efficiency of the tidal energy conversion. There is no contradiction between
 395 these two tendencies. Analysis of Figure 4 c and 4 d shows that the coarser
 396 grids incorporate larger volumes of water with the increase of the grid step.
 397 In fact, with the coarser grids, the topography's tidal activity is different
 398 from that simulated over the fine-resolution topography.

399 A series of numerical experiments were also conducted to test the model
 400 output's sensitivity to the choice of diffusivity/viscosity model coefficients.

Water mixing parameterization is critical for accurately modelling various processes, from microscopic to global atmospheric and oceanic scales. In the present study, we used the Richardson-number dependent parameterization scheme PP81. This turbulent closure scheme provides the APE saturation over eight tidal cycles. The Osborn relation based scheme KL10 also revealed a similar performance over 7.5 tidal periods. Note that its further performance over ten tidal cycles did not demonstrate any tendency to reach the stationary level. In general, the usage of two vertical turbulent mixing schemes, PP81 and KL10, did not significantly differ the model output over several tidal cycles, although the KL10 closure model shows a higher internal tidal energy saturation level.

6. Acknowledgement

This work was supported by the Natural Environment Research Council (NERC) [grant NE/K011855/1]. The authors thank the University of Plymouth Research Computing Service staff for their support.

References

- Adcroft, A., C. Hill, and J. Marshall (1997) Representation of topography by shaved cells in a height coordinate Ocean Model. *Monthly Weather Review*, 125(9), 2293-2315, doi:10.1175/1520-0493(1997)125<2293:ROTBSC>2.0.CO;2.
- Baum J.K., R.A. Maiers, D.G. Kehler, B.Warm, S.Harley, and P.Doherty (2003) Collapse and conservation of shark populations in the Northwest Atlantic. *Science*, 299, 389–392.
- Egbert, G.D., and S.Y. Erofeeva (2002) Efficient inverse modeling of barotropic ocean tides, *J. Atmos. Oceanic Technol.*, 19(2), 183–204.
- Gill, A.E. (1982) Atmosphere-Ocean Dynamics. Academic Press, 662pp.
- Gregg, M.C. (1989) Scaling turbulent dissipation in thermocline. *J. Geophys. Res.*, 92, 5249-5286.
- Hampton J., J.R. Sibert, P. Kleiber, M.N. Maunder, S.R. Harley (2005) Fisheries: Decline of Pacific tuna populations exaggerated? *Nature*, 434, E1–E2.

- 432 Holliday, D., and M.E. McIntyre (1981) On potential energy density in an
433 incompressible fluid. *J. Fluid Mech.*, *107*, 221-225.
- 434 Kang, D., and O. Fringer (2010) On the calculation of available potential
435 energy in internal wave fields. *J. Phys. Oceanogr.*, *40*, 2539-2545.
- 436 Kelly, S.M., J.D. Nash, and E. Kunze (2010) Internal-tide energy over to-
437 pography. *J. Geophys. Res.*, *115*, C06014, doi:10.1029/2009JC005618.
- 438 Klymak, J.M., and S.M. Legg (2010) A simple mixing scheme for models
439 that resolve breaking internal waves. *Ocean Modelling*, *33*, 224-234.
- 440 Klymak, J.M., M. Buijsman, S. Legg, and R. Pinkel (2013) Parameterizing
441 surface and internal tide scattering and breaking on supercritical topogra-
442 phy: the one- and two-ridge cases. *J. Phys. Oceanogr.*, *43*, 1380-1397.
- 443 Ledwell, J.R., A.J. Watson, and C.S. Law (1998) Mixing of the tracer in the
444 pycnocline. *J. Geophys. Res.*, *103*, 21499-21529.
- 445 Lerczak, J.A., and C.D. Winant, and M.C. Hendershott (2003) Observations
446 of the semidiurnal internal tide on the southern California slope and shelf.
447 *J. Geophys. Res.*, *108*(C3), doi:10.1029/2001JC001128.
- 448 Lorenz, E.N. (1955) Available potential energy and the maintenance of the
449 general circulation. *Tellus*, *7*, 157-167.
- 450 Marshall, J., A. Adcroft, C. Hill, L. Perelman, and C. Heisey (1997), A
451 finite-volume, incompressible Navier-Stokes model for studies of the ocean
452 on parallel computers. *J. Geophys. Res.*, *102*, 5733-5752.
- 453 MacKinnon, J. A. et al. (2017) Climate process team on internal-wave driven
454 ocean mixing. *Bull. Am. Meteor. Soc.*, *98*, 2429-2454.
- 455 Munk W. and C. Wunsch (1998) Abyssal recipes II: energetics of tidal and
456 wind mixing *Deep Sea Res.*, *45*, 1997-2010.
- 457 Myers, N, R.A. Mittermeier, C.G. Mittermeier, G.A.B. da Fonseca, J. Kent
458 (2000) Biodiversity hotspots for conservation priorities. *Nature*, *403*,
459 853-858.
- 460 Myers R.A., B. Worm (2003) Rapid worldwide depletion of predatory fish
461 communities. *Nature* *423*, 280-283.

462 Niwa, Y., and T. Hibiya (2011) Estimation of baroclinic tide energy avail-
463 able for deep ocean mixing based on three-dimensional global numerical
464 simulations. *J. Oceanogr.*, *67*, 493-502.

465 Osborn, T.R.(1980) Estimates of the local rate of vertical diffusion from
466 dissipation measurements. *J. Phys. Oceanogr.*, *10*, 83-89.

467 Pacanowski, R.C., and S.G.H. Philander (1981) Parameterisation of vertical
468 mixing in numerical models of Tropical Oceans. *J. Phys. Oceanogr.*, *11*,
469 1443-1451.

470 Plozin, K.L., J.M.Toole, J.R. Ledwell, and R.W.Schmitt (1997) Spatial vari-
471 ability of turbulent mixing in the abyssal ocean. *Science*, *276*, 93-96.

472 Robertson, R. (2006). Modeling internal tides over Fieberling Guyot: Res-
473 olution, parameterization, performance. *Ocean Dynamics*, *56*, 430– 444.
474 <https://doi.org/10.1007/s10236-006-0062-5>.

475 Roberts, C.M. (2002) Priorities for tropical reefs marine biodiversity hotspots
476 and conservation. *Science*, *295*, 1280–1284.

477 Stashchuk, N., V. Vlasenko, M.E. Inall, and D. Aleynik (2014) Horizontal
478 dispersion in shelf seas: High resolution modelling as an aid to sparse
479 sampling. *Progr. Oceanogr.*, *128*, 74-87.

480 Stashchuk, N., and V. Vlasenko (2017) Bottom trapped internal waves over
481 the Malin Sea continental slope. *Deep-Sea Res. I*, *119*, 68-80.

482 Stashchuk, N., V. Vlasenko, P. Hosegood, and A.W. Nimmo-Smith (2017)
483 Tidally induced residual current over the Malin Sea continental slope.
484 *Cont. Shelf. Res.*, *139*, 21-34.

485 Stashchuk, N., V. Vlasenko, and K. L. Howell (2018) Modelling tidally in-
486 duced larval dispersal over Anton Dohrn Seamount. *Ocean Dyn.*, *68(11)*,
487 1515-1526.

488 Stashchuk, N., and V. Vlasenko (2021) Internal wave dynamics over isolated
489 seamount and its influence on coral larvae dispersion. *Fronties.*, *123(9)*,
490 6753-6765.

491 Vic, C., A. C. Naveira Garabato, J. A. M. Green, A. F. Waterhouse, Z. Zhao,
 492 A. Melet, C. de Lavergne, M. C. Buijsman, and G. R. Stephenson (2019)
 493 Deep-ocean mixing driven by small-scale internal tides. *Nature Communi-*
 494 *cations*—, 10, 2099, doi.org/10.1038/s41467-019-10149-5.

495 Vitousek, S. and O.B. Fringer (2011) Physical vs. numerical dispersion in
 496 nonhydrostatic ocean modeling. *Ocean Model.*, 40, 72-86.

497 Vlasenko, V., N. Stashchuk, M.E. Inall, M. Porter, and D. Aleynik (2016)
 498 Focusing of baroclinic tidal energy in a canyon. *J. Geophys. Res.*, 121(4),
 499 2824-2840.

500 Vlasenko, V., N. Stashchuk, W.A.M. Nimmo-Smith (2018) Three-
 501 dimensional dynamics of baroclinic tides over a seamount. *J. Geophys.*
 502 *Res.*, 123(2), 1263-1285.

503 Vlasenko, V., and N. Stashchuk (2018) Tidally induced overflow of the
 504 Faroese channels bottom water over the Wyville Thomson Ridge. *J. Geo-*
 505 *phys. Res.*, 123(9), 6753-6765.

506 Vlasenko, V., and N. Stashchuk (2021) Setting tidal forcing for re-
 507 gional modelling of internal waves. *Ocean modelling*, 160, 101767.
 508 <https://doi.org/10.1016/j.ocemod.2021.101767>.
 509 bibitem[Vlasenko et al.(2005)]Vletal2005 Vlasenko, V., N. Stashchuk, and
 510 K. Hutter (2005) Baroclinic tides: theoretical modeling and observational
 511 evidence. Cambridge University Press.

512 Vlasenko, V., N. Stashchuk, M.E. Inall, and J. Hopkins (2014) Tidal en-
 513 ergy conversion in a global hot spot: On the 3-D dynamics of baroclinic
 514 tides at the Celtic Sea shelf break. *J. Geophys. Res.*, 119, doi:10.1002/
 515 2013JC009708.

516 Worm B, H.K. Lotze, R.A. Myers (2003) Predator diversity hotspots in the
 517 blue ocean. *Proc. Natl. Acad. Sci. USA* 100:9884–9888.

518 Zhang, L., M.C. Buijsman, E. Comino, and H. L. Swinney (2017) Internal
 519 wave generation by tidal flow over periodically and randomly distributed
 520 seamounts. *J. Geophys. Res.*, 122, 5063-5074, doi:10.1002/2017JC012884.

521 Zilberman, N. V., and J. M. Becker, M. A. Merrifield, and G. S.
522 Carter (2009) Model estimates of M2 internal tide generation over Mid-
523 Atlantic Ridge topography. *J. Phys. Oceanogr.* , *39(10)*, 2635-2651,
524 doi:10.1175/2008JPO4136.1

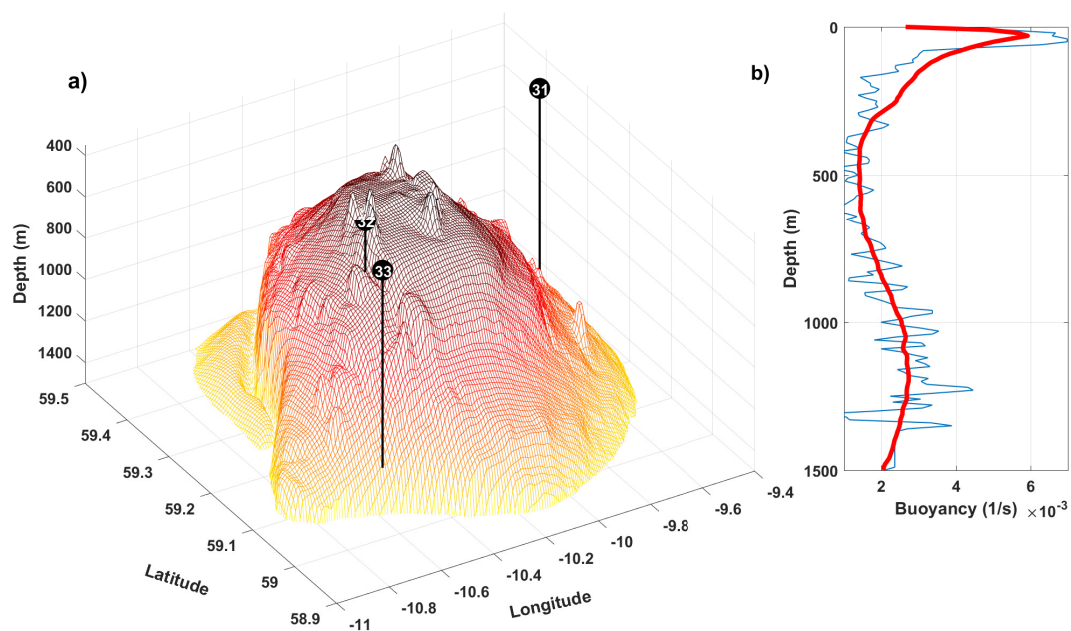


Figure 1: a) Bottom topography of Rosemary Bank Seamount (RBS) with the location of CTD stations 31, 32, and 33 conducted during the 136th cruise of the RV "James Cook". b) The buoyancy frequency recorded in the RBS area is shown in blue. The smoothed buoyancy frequency profile used in the modelling is shown in red.

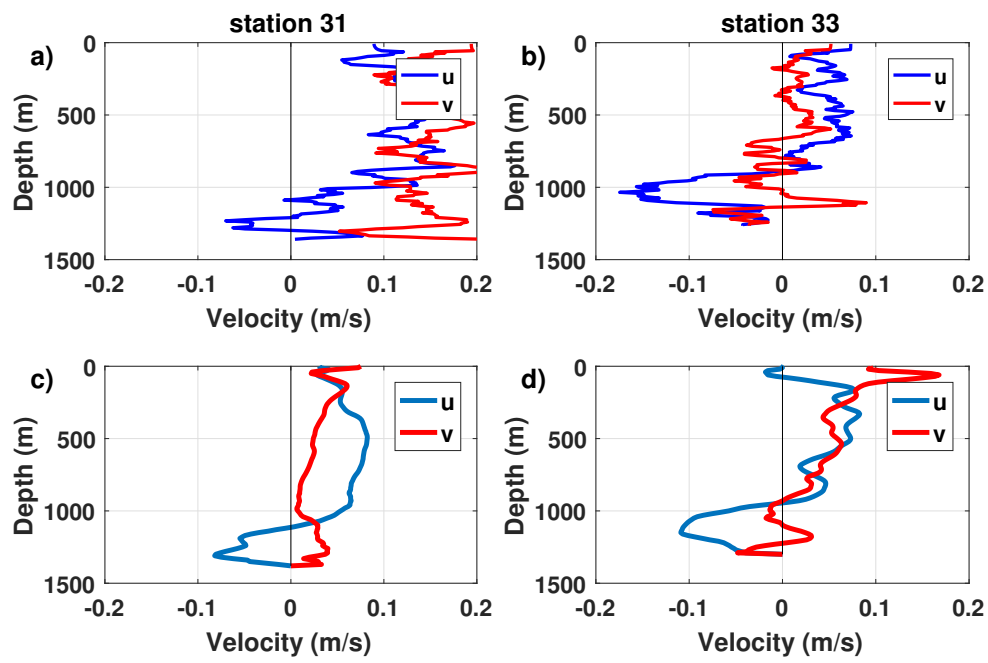


Figure 2: Vertical profiles of zonal (blue) and meridional (red) velocities recorded by the LADCP at 31-st and 33-rd CTD stations (panels a and b, respectively). Panels c and d present the same profiles but replicated by the numerical model.

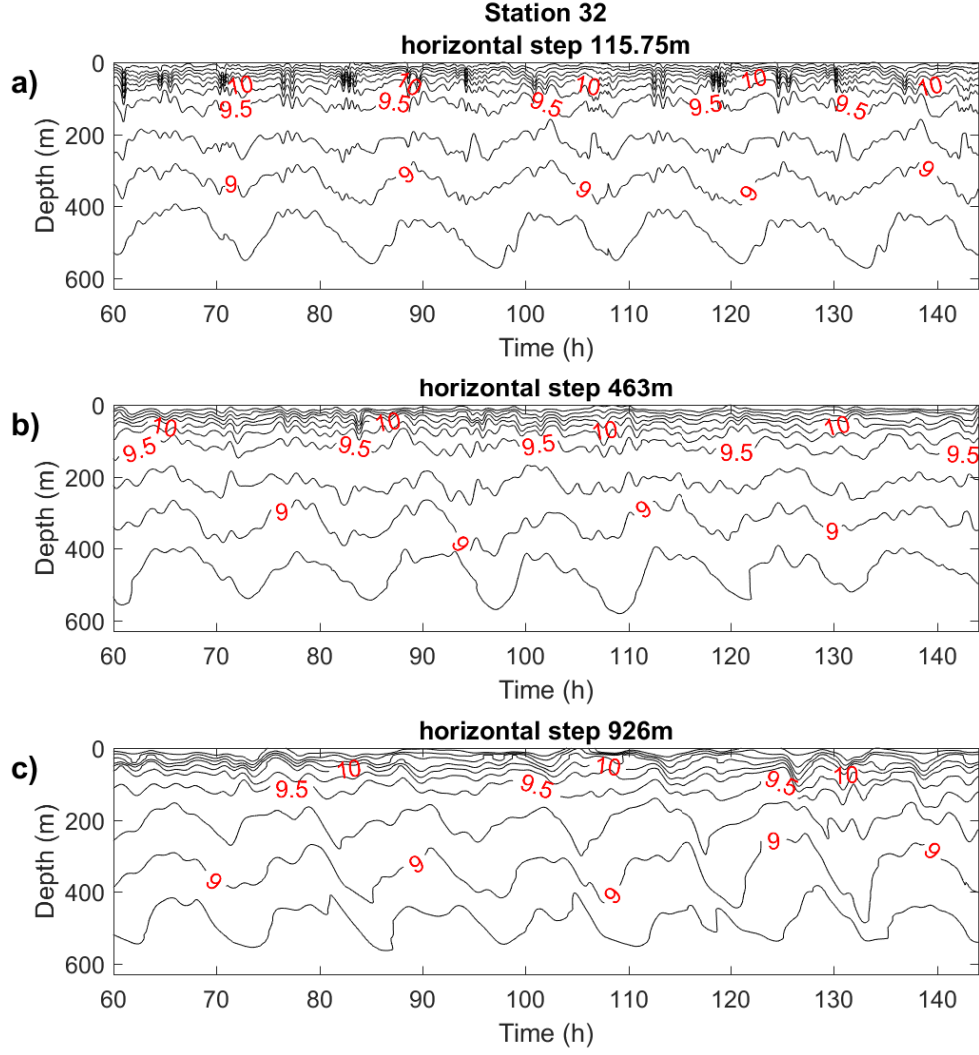


Figure 3: Temperature time series reproduced by the MITgcm at the 32-nd CTD station (the position is shown in Figure 1). The horizontal grid step in these experiments was 115.75 m, 463 m, and 926 m (panels a, b, c, respectively).

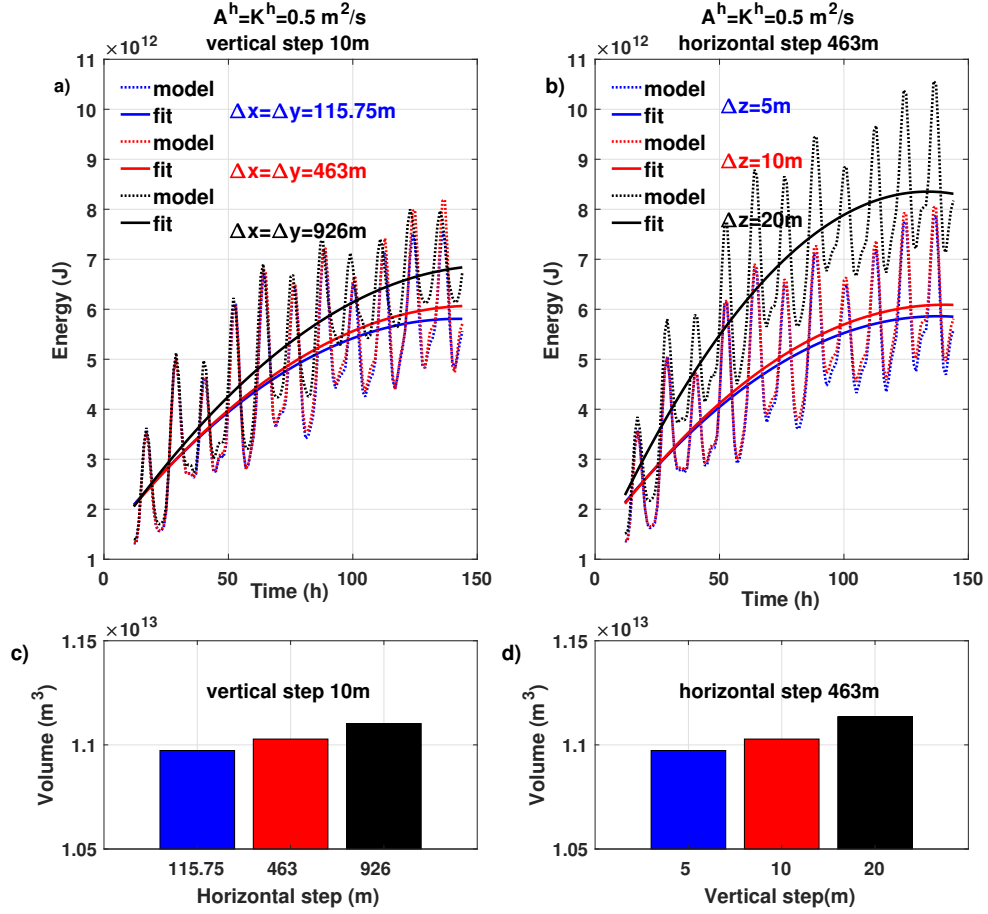


Figure 4: a) Model predicted available potential energy (APE) calculated for the RBS area with a different vertical grid resolution: 115.75m (blue), 463m (red) and 926m (black). b) The same, but calculated with different vertical steps: 5m (blue), 10m (red) and 20m (black). c) and d) The volume of the model domain calculated for different horizontal and vertical grid resolutions. The values are shown in the graph.

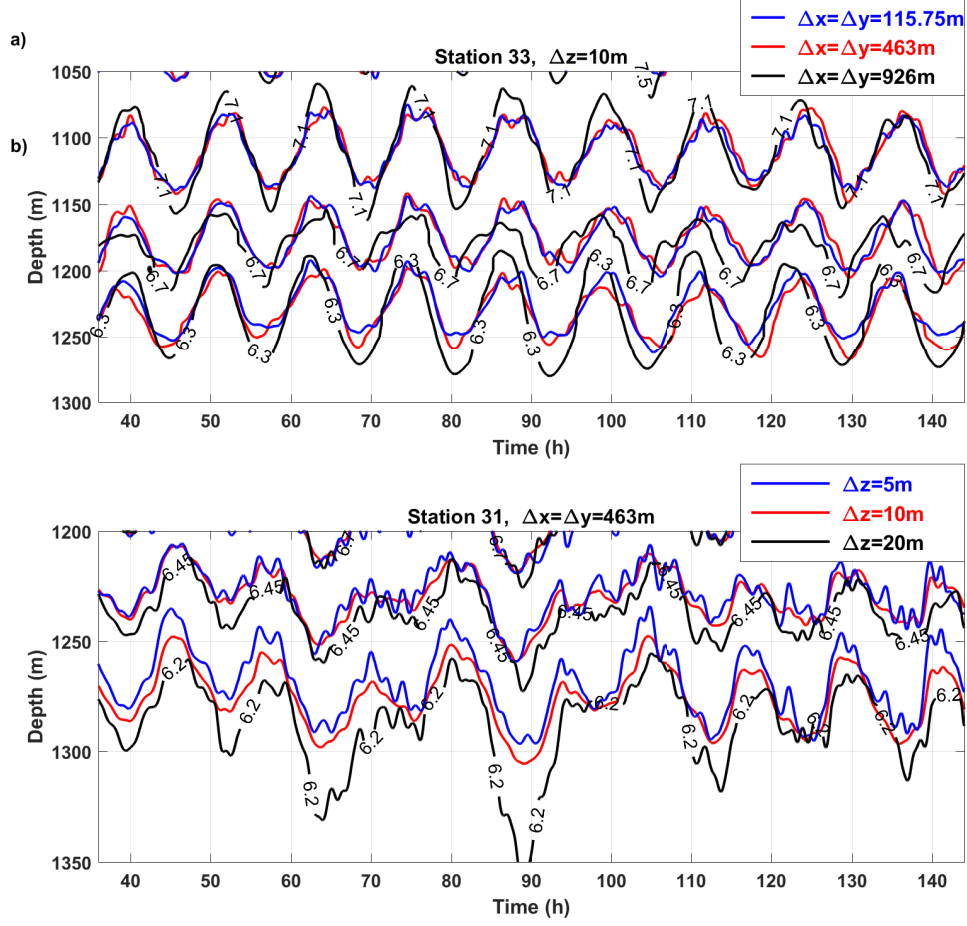


Figure 5: The model predicted time series at stations 33 a) and 31 b) for different horizontal a) and vertical b) grid steps. The model resolution is detailed in the figure legend.

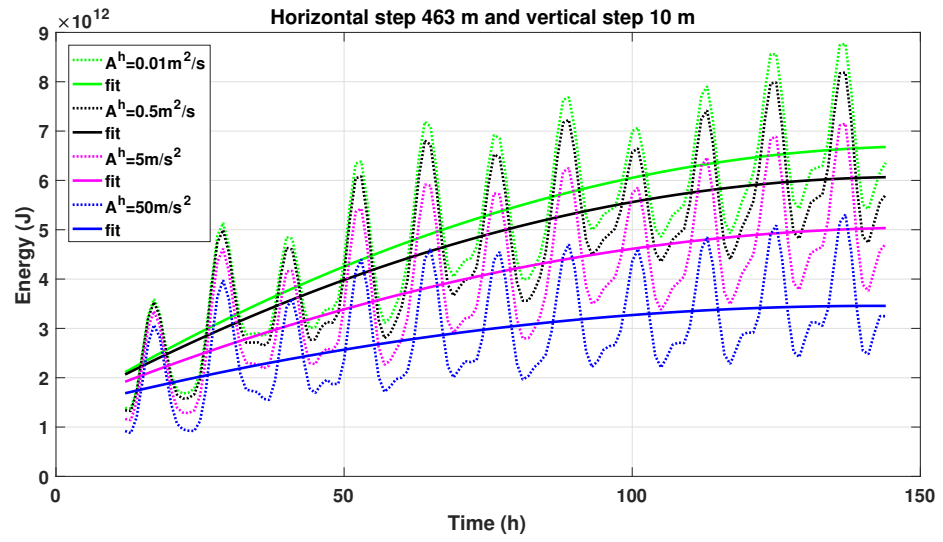


Figure 6: The domain integrated APE calculated for different values of horizontal viscosity coefficient.

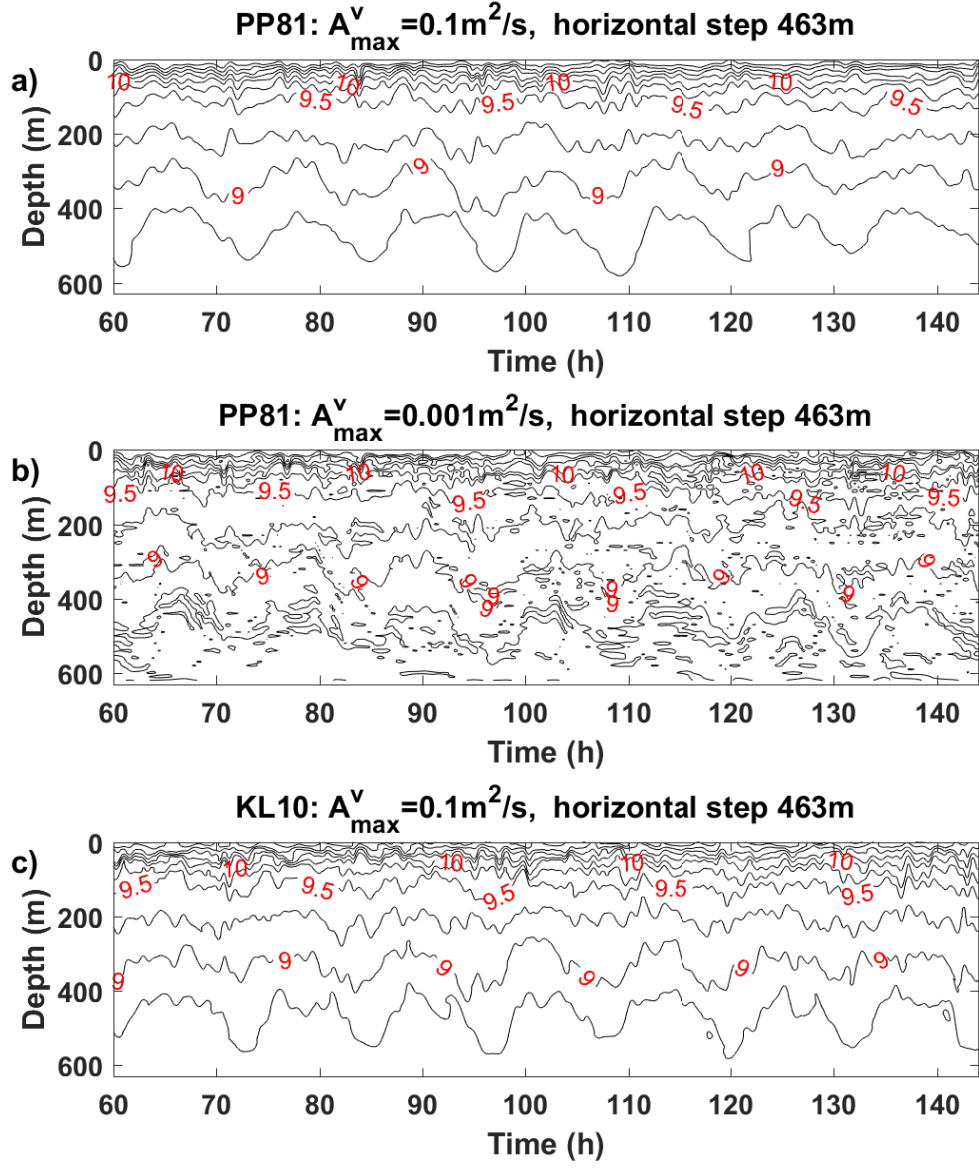


Figure 7: Sensitivity runs conducted with different vertical mixing parameterization schemes. The model predicted temperature time series were calculated for the point of CTD station 32 (Figure 1).

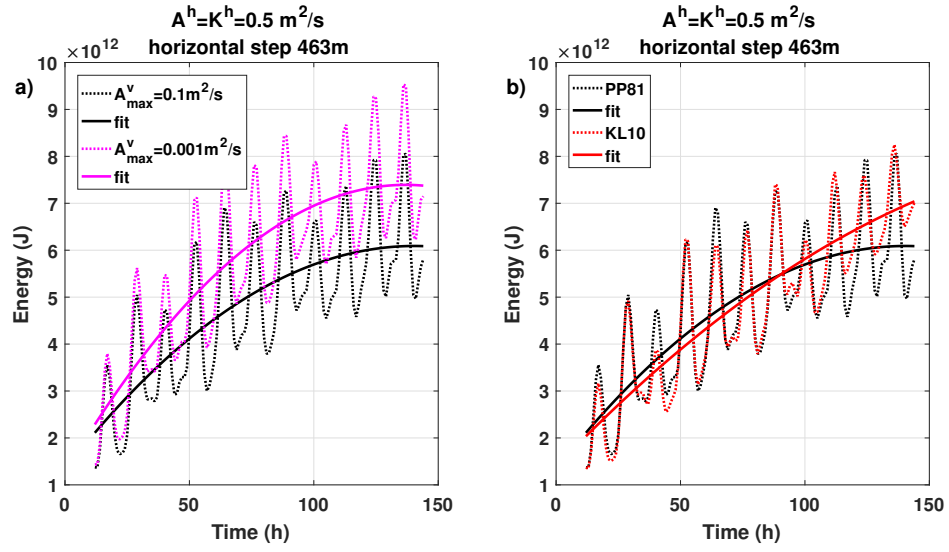


Figure 8: The domain integrated APE time series for different viscosity coefficients and parameterization schemes (Pacanowski and Philander (1981) and Klymak et al. (2013)) calculated at the position of CTD station 32.